

# Suppression of the charge fluctuations by nonlocal correlations close to the Mott transition

Irakli Titvinidze,<sup>1</sup> Julian Stobbe,<sup>1</sup> Marvin Leusch,<sup>1</sup> and Georg Rohringer<sup>2,1</sup>

<sup>1</sup>*Institute of Theoretical Physic, University of Hamburg, 20355 Hamburg, Germany*

<sup>2</sup>*Theory and Simulation of Condensed Matter, Department of Physics,  
King's College London, The Strand, London WC2R 2LS, United Kingdom*

(Dated: July 18, 2025)

In this paper, we investigate the impact of nonlocal correlations on charge fluctuations in the two-dimensional single-band Hubbard model close to the Mott metal-to-insulator transition. At half-filling and for interaction strengths and temperatures where the system is in the Mott insulating phase, charge fluctuations are strongly suppressed. Under these conditions, dynamical mean-field theory (DMFT) calculations predict a strong enhancement of the charge susceptibility at small (electron or hole) doping. However, these DMFT results include only the effects of purely local correlations despite the importance of nonlocal correlations in two-dimensional systems. We have, hence, carried out dynamical vertex approximation (DFA) simulations which allow for the inclusion of such nonlocal correlation effects while retaining the local ones of DMFT. Our numerical data show that close to half-filling the large uniform charge susceptibility of DMFT is strongly suppressed by nonlocal fluctuations but gradually increases with (electron) doping. At a certain doping value charge fluctuations become eventually larger in DFA with respect to DMFT indicating that the absence of nonlocal correlations underestimates the mobility of the charge carriers in this parameter regime. This metallization effect is also reflected in an enhancement of the DFA kinetic and potential energies and a corresponding reduction of the (absolute value of the) DFA Matsubara self-energy with respect to DMFT.

## I. INTRODUCTION

Strongly correlated electron systems feature a wide range of interesting physical phenomena including interaction-driven metal-to-insulator transitions<sup>1–4</sup>, strange metal behavior<sup>5,6</sup> or Hund's physics<sup>7–9</sup>. A particularly interesting effect in this type of material is the collective excitations of the constituent particles. In fact, due to their (strong) mutual interactions single electrons can form larger entities whose physical properties are substantially different from the underlying building blocks. P. A. Anderson summarized this emergence of new phenomena from well understood fundamental components (i.e., the electrons) in his famous article “More Is Different”.<sup>10</sup> Examples for collective excitations are spin<sup>11–13</sup>, pairing<sup>14,15</sup>, nematic<sup>16,17</sup> or excitonic<sup>18</sup> fluctuations. Another important type of collective behavior in many-electron systems is charge fluctuations, which can be observed, for instance, in high-temperature superconductors<sup>19</sup>, excitonic insulators<sup>20</sup> or systems with pronounced long-range Coulomb interactions such as adatoms on Si surfaces<sup>21</sup>.

The theoretical description and understanding of such phenomena in realistic strongly correlated electron systems is, however, very challenging due to the strong interaction between the particles which prevents an effective independent-particle description. In most cases, an exact solution is unattainable, and one must rely on (i) simplified models and (ii) approximate methods. A prime example of the first point is the single-band Hubbard Hamiltonian<sup>22–25</sup>. Despite being one of the simplest models for correlated electrons (approximating the Coulomb repulsion as a single scalar value) it entails

a rich variety of physical phenomena including collective fluctuations in the spin, pairing and, in particular, the charge sector. Yet, a rigorous analytical or (at least) numerical solution is available only in very specific cases, for instance in one spatial dimension where Bethe Ansatz<sup>26,27</sup>, density matrix renormalization group or matrix product states<sup>28–30</sup> provide exact results. In this respect, DMFT<sup>31–33</sup> has been a huge step forward as it non-perturbatively captures all purely local correlation effects in the system by means of a local but frequency-dependent dynamical self-energy (which is indeed the exact solution in infinite spatial dimensions<sup>32</sup>). One of the biggest successes of DMFT is the accurate quantitative description of the correlation-driven Mott metal-to-insulator transition in correlated model systems<sup>31</sup> and real materials<sup>34,35</sup>. While this Mott transition occurs exactly at half-filling, fascinating physical phenomena are observed in the (electron or hole) doped Mott insulator, which is believed to capture important aspects of high-temperature superconductors<sup>36</sup>. In particular, for small deviations of the particle density from unity, a strong increase of the uniform charge susceptibility<sup>37,38</sup> (proportional to the compressibility) is observed which eventually diverges at the critical endpoint of the Mott transition within the DMFT framework. This is quite surprising as for a one-band model with a purely repulsive local interaction, a suppression of charge fluctuations could be expected for large coupling strength. It has been recently demonstrated that this enhancement of charge fluctuations is indeed an emergent phenomenon which is associated with a divergence of the local irreducible charge vertex of DMFT<sup>39,40</sup> which leads to an effective *attractive* interaction between the particles, thus enhanc-

ing collective charge excitations.

It is, however, not obvious to which extent the enhancement of the charge fluctuations is associated with the local DMFT approximation. In fact, DMFT neglects nonlocal correlations, which can certainly play a crucial role in finite dimensions. Particularly in low-dimensional systems long-wavelength collective fluctuations become important, especially in the vicinity of transitions to spatially ordered phases. A good example is the two-dimensional Hubbard model, for which DMFT incorrectly predicts long-range antiferromagnetic order in contradiction with the Mermin-Wagner theorem, that excludes continuous symmetry breaking solutions at finite temperatures. Moreover, nonlocal correlations are believed to be essential near the Mott metal-to-insulator transition, which is not prohibited by the Mermin-Wagner theorem and may indeed occur in two-dimensional systems. Capturing these nonlocal effects is therefore indispensable for a realistic description of strongly correlated electrons, and in particular the above mentioned charge fluctuations, in low dimensions. To overcome these limitations of DMFT, several cluster and diagrammatic extensions of DMFT have been developed. These include the cellular DMFT (CDMFT)<sup>41–43</sup>, the dynamical cluster approximation (DCA)<sup>43–45</sup>, the dual fermion (DF)<sup>46–48</sup>, dual boson (DB)<sup>48–50</sup> and one-particle-irreducible (1PI)<sup>51</sup> approaches, the TRILEX<sup>52,53</sup> and QUADRILEX<sup>54</sup> methods, and the dynamical vertex approximation (DFA)<sup>48,55–59</sup>. These methods incorporate nonlocal correlations on top of the local DMFT solution and have led to significant progress in the theoretical understanding of correlated systems in two and three dimensions.

In this paper, our goal is to investigate the impact of nonlocal correlations on the enhancement of charge fluctuation predicted by DMFT for the two-dimensional Hubbard model on a square lattice with nearest-neighbor, next-nearest-neighbor, and next-to-next-nearest-neighbor hopping, in the regime close to the Mott transition. For this purpose, we employ the dynamical vertex approximation (DFA) in its ladder formulation<sup>51,56,57</sup> which systematically includes nonlocal correlations beyond DMFT. More specifically, we exploit a recently developed improved version of this method<sup>58</sup> to analyze the doping dependence of the (uniform) charge susceptibility  $\chi_{d,\mathbf{q}=0}^{\omega=0}$ . This extension of the previous versions of the method allows for a consistent renormalization between both spin and charge fluctuations and is, hence, particularly suitable for this task. Our DFA calculations predict a substantial suppression of the large charge fluctuations close to half-filling and an enhancement at larger doping with respect to the DMFT prediction. Hence, DMFT overestimates the dynamics of charge degrees of freedom for densities close to unity while it seems to underestimate it for larger fillings. This picture is also supported by the study of the spin susceptibility and the momentum-resolved self-energy at the Fermi surface, which offer complementary insights into

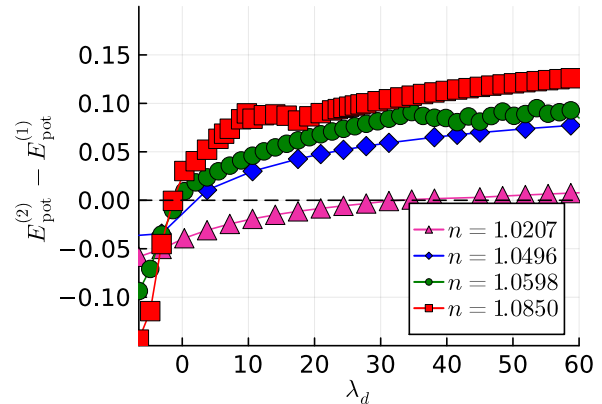


FIG. 1. Difference between the potential energies obtained from two- and one-particle correlation functions on the left and right hand sides of Eq. (11b), respectively, as a function of  $\lambda_d$  where  $\lambda_m$  is determined (for a given  $\lambda_d$ ) from Eq. (11a). Crossing with the  $x$ -axes corresponds to the solution of Eqs. (11). Data are shown for  $U = 2.64$  and  $\beta = 44.0$  (see Fig. 2 and discussion in Sec. III A) for four different values of the filling  $n$ .

the interplay between spin and charge degrees of freedom. Furthermore, our findings are also confirmed by the behavior of the kinetic and potential energies as a function of doping.

The paper is organized as follows. In Sec. II, we introduce the Hubbard model and key aspects of the ladder DFA (lDFA) method used in this study. In Sec. III, we present our numerical results. In particular, Secs. III A and III C discuss the behavior of the charge and spin susceptibilities as a function of filling, respectively. We complete these investigations by an analysis of the correlation length of the charge fluctuations in Sec. III B. In Sec. III D, we examine the self-energy at the Fermi surface, and in Sec. III E, we analyze the kinetic and potential energies. We conclude our paper with a summary and outlook in Sec. IV and provide more details about the uniform charge susceptibility and the self-energy in the entire Brillouin zone in appendices A and B.

## II. MODEL AND METHOD

### A. Model

We study the two-dimensional Hubbard model on a square lattice with nearest-neighbor ( $t$ ), next-nearest-neighbor ( $t'$ ), and next-to-next-nearest-neighbor ( $t''$ ) hopping, along with a local Hubbard interaction  $U$ . The Hamiltonian is given by

$$\hat{\mathcal{H}} = - \sum_{i,j,\sigma} t_{ij} \hat{c}_{i\sigma}^\dagger \hat{c}_{j\sigma} + U \sum_i \hat{n}_{i\uparrow} \hat{n}_{i\downarrow}. \quad (1)$$

Here,  $\hat{c}_{i\sigma}^\dagger$  ( $\hat{c}_{i\sigma}$ ) creates (annihilates) an electron with spin  $\sigma$  at lattice site  $i$ , and  $\hat{n}_{i\sigma} = \hat{c}_{i\sigma}^\dagger \hat{c}_{i\sigma}$  is the local particle number (or density) operator. The corresponding dispersion relation is

$$\varepsilon_{\mathbf{k}} = -2t(\cos(\mathbf{k}_x) + \cos(\mathbf{k}_y)) - 4t' \cos(\mathbf{k}_x) \cos(\mathbf{k}_y) - 2t''(\cos(2\mathbf{k}_x) + \cos(2\mathbf{k}_y)), \quad (2)$$

where we set  $t = 0.25\text{eV}$  which implies that the half bandwidth  $D = 4t = 1\text{eV}$  which we use as unit of energy. We select hopping parameters commonly used for cuprates, setting  $t' = -0.3t$  and  $t'' = 0.2t$  although this choice has no specific significance in the context of this paper since we are conducting a model study without any reference to a specific material. In the following we will work in Matsubara frequency space where fermionic and bosonic Matsubara frequencies are denoted by  $\nu = (2n+1)\pi/\beta$  and  $\omega = 2\pi m/\beta$ , respectively, where  $\beta = 1/T$  is the inverse temperature and  $n, m \in \mathbb{Z}$ . For readability and brevity, integrals over momenta  $\mathbf{k}$  within the Brillouin zone (BZ) are written as  $\frac{1}{V_{\text{BZ}}} \int_{\text{BZ}} d\mathbf{k} \equiv \sum_{\mathbf{k}}$ .

## B. Ladder DGA

The DGA approach was originally developed in Ref.56, with its ladder approximation introduced in Refs. 55–58. This diagrammatic extension of DMFT constructs a non-local self-energy from the DMFT starting point through the (Schwinger-Dyson) equation of motion (EOM)

$$\Sigma_{\mathbf{k}}^\nu = \frac{Un}{2} - \frac{U}{\beta^2} \sum_{\nu', \omega, \mathbf{k}', \mathbf{q}} F_{\uparrow\downarrow, \mathbf{k}\mathbf{k}'; \mathbf{q}}^{\nu\nu'\omega} G_{\mathbf{k}'}^{\nu'} G_{\mathbf{k}'+\mathbf{q}}^{\nu'+\omega} G_{\mathbf{k}+\mathbf{q}}^{\nu+\omega}. \quad (3)$$

where the full vertex function  $F_{\uparrow\downarrow, \mathbf{k}\mathbf{k}'; \mathbf{q}}^{\nu\nu'\omega}$  is obtained from the two-particle fully irreducible vertex  $\Lambda_{\sigma\sigma'}^{\nu\nu'\omega}$  of DMFT via the Bethe-Salpeter and parquet equations in all scattering channels<sup>60–63</sup>. While this approach correctly captures the mutual screening effects between charge, spin and particle-particle fluctuations and, hence, fulfills the associated sum rules, it is typically restricted to rather high temperatures due to its numerical complexity (in spite of a number of improvements which have been introduced in previous years<sup>64,65</sup>). To simplify the procedure one can neglect this mutual renormalization between the scattering channels induced by the parquet equations and construct the generalized susceptibilities  $\chi_{r, \mathbf{q}}^{\nu\nu'\omega}$  in the most relevant channels  $r$  [which are  $r=d$  density (or charge) and  $r=m$  magnetic (or spin) channels in the case of a repulsive interaction] in a one-shot calculation from the local two-particle vertices  $\Gamma_r^{\nu\nu'\omega}$ , which are irreducible only in channel  $r$ , via the respective Bethe-Salpeter equations:

$$\chi_{r, \mathbf{q}}^{\nu\nu'\omega} = \beta \chi_{0, \mathbf{q}}^{\nu\omega} \delta_{\nu\nu'} - \frac{1}{\beta} \chi_{0, \mathbf{q}}^{\nu\omega} \sum_{\nu_1} \Gamma_r^{\nu\nu_1\omega} \chi_{r, \mathbf{q}}^{\nu_1\nu'\omega}. \quad (4)$$

Here, the bubble term  $\chi_{0, \mathbf{q}}^{\nu\omega} = -\sum_{\mathbf{k}} G_{\mathbf{k}}^\nu G_{\mathbf{k}+\mathbf{q}}^{\nu+\omega}$  is just the convolution of two DMFT Green's functions

$$G_{\mathbf{k}}^\nu = \frac{1}{i\nu + \mu_{\text{DMFT}} - \varepsilon_{\mathbf{k}} - \Sigma_{\mathbf{k}}^\nu} \quad (5)$$

in momentum space, where  $\Sigma_{\mathbf{k}}^\nu$  denotes the local DMFT self-energy and  $\mu_{\text{DMFT}}$  refers to the chemical potential, which determines the filling  $n$ .

Within this ladder version of DGA (referred to as LDGA in the following) the EOM (3) can be then recast in terms of the physical susceptibilities  $\chi_{r, \mathbf{q}}^\omega$  and the triangular vertices  $\gamma_{r, \mathbf{q}}^{\nu\nu'\omega}$  of DMFT which are obtained from the generalized susceptibilities  $\chi_{r, \mathbf{q}}^{\nu\nu'\omega}$  as

$$\chi_{r, \mathbf{q}}^\omega = \frac{1}{\beta^2} \sum_{\nu, \nu'} \chi_{r, \mathbf{q}}^{\nu\nu'\omega}, \quad (6a)$$

$$\gamma_{r, \mathbf{q}}^{\nu\omega} = [\chi_{0, \mathbf{q}}^{\nu\omega} (1 \pm U \chi_{r, \mathbf{q}}^\omega)]^{-1} \frac{1}{\beta} \sum_{\nu'} \chi_{r, \mathbf{q}}^{\nu\nu'\omega} \quad (6b)$$

The EOM for the non-local LDGA self-energy then becomes

$$\Sigma_{\mathbf{k}}^\nu = \frac{Un}{2} - \frac{U}{\beta} \sum_{\omega, \mathbf{q}} \left[ 1 + \frac{1}{2} \gamma_{d, \mathbf{q}}^{\nu\omega} (1 - U \chi_{d, \mathbf{q}}^\omega) - \frac{3}{2} \gamma_{m, \mathbf{q}}^{\nu\omega} (1 + U \chi_{m, \mathbf{q}}^\omega) - \frac{1}{\beta} \sum_{\nu'} \chi_{0, \mathbf{q}}^{\nu'\omega} F_{m, \mathbf{q}}^{\nu\nu'\omega} \right] G_{\mathbf{k}+\mathbf{q}}^{\nu+\omega}, \quad (7)$$

where  $F_m^{\nu\nu'\omega}$  is the full local vertex of DMFT in the magnetic (spin) channel.

While the numerical complexity of the LDGA scheme is substantially reduced with respect to the full parquet based DGA it violates specific consistency relations due to the absence of a self-consistent mutual renormalization of different scattering channels. In particular, the following two equations for the physical susceptibilities defined in Eq. (6a) are typically *not* fulfilled within LDGA:

$$\frac{1}{2\beta} \sum_{\omega, \mathbf{q}} (\chi_{d, \mathbf{q}}^\omega + \chi_{m, \mathbf{q}}^\omega) = \frac{n}{2} \left( 1 - \frac{n}{2} \right) \quad (8a)$$

$$\underbrace{\frac{1}{2\beta} \sum_{\omega, \mathbf{q}} (\chi_{d, \mathbf{q}}^\omega - \chi_{m, \mathbf{q}}^\omega)}_{E_{\text{pot}}^{(2)}} + \frac{Un^2}{4} = \underbrace{\frac{1}{\beta} \sum_{\nu, \mathbf{k}} G_{\mathbf{k}}^\nu \Sigma_{\mathbf{k}}^\nu}_{E_{\text{pot}}^{(1)}}, \quad (8b)$$

where  $\Sigma_{\mathbf{k}}^\nu$  is the LDGA self-energy obtained via Eq. (7) and

$$G_{\mathbf{k}}^\nu = \frac{1}{i\nu + \mu_{\text{DGA}} - \varepsilon_{\mathbf{k}} - \Sigma_{\mathbf{k}}^\nu} \quad (9)$$

is the LDGA Green's function. The relation (8a) is a consequence of the Pauli principle while the second equation (8b) corresponds to the consistency of the potential energy when it is obtained from one- ( $E_{\text{pot}}^{(1)}$ ) and two-particle ( $E_{\text{pot}}^{(2)}$ ) correlation functions, respectively.

A restoration of these consistency relations has been demonstrated to reintroduce a re-balancing between the spin and charge channel and improve the predictive power of IDGA in the three-dimensional Hubbard model<sup>58</sup>. This restoration of the consistency relations (8) is efficiently possible within the IDGA approach by following Moriya's theory of itinerant magnetism<sup>11,55,57</sup>. Here, the physical susceptibilities  $\chi_{d,\mathbf{q}}^\omega$  and  $\chi_{m,\mathbf{q}}^\omega$  are renormalized by static parameters  $\lambda_d$  and  $\lambda_m$ :

$$\chi_{r,\mathbf{q}}^{\lambda_r,\omega} = \left( \frac{1}{\chi_{r,\mathbf{q}}^\omega} + \lambda_r \right)^{-1}, \quad (10)$$

which corresponds to a renormalization of the correlation length of the corresponding fluctuations [see Ref. 58 and Eq. (14) in Sec. III B]. The parameters  $\lambda_d$  and  $\lambda_m$  are then chosen in such a way that the consistency relations in Eqs. (8) are satisfied, leading to

$$\frac{1}{2\beta} \sum_{\mathbf{q}} \left( \chi_{d,\mathbf{q}}^{\lambda_d,\omega} + \chi_{m,\mathbf{q}}^{\lambda_m,\omega} \right) \stackrel{!}{=} \frac{n}{2} \left( 1 - \frac{n}{2} \right) \quad (11a)$$

$$\frac{U}{2\beta} \sum_{\mathbf{q}} \left( \chi_{d,\mathbf{q}}^{\lambda_d,\omega} - \chi_{m,\mathbf{q}}^{\lambda_m,\omega} \right) + U \frac{n^2}{4} \stackrel{!}{=} \frac{1}{\beta} \sum_{\nu,\mathbf{k}} G_{\mathbf{k}}^{\lambda,\nu} \Sigma_{\mathbf{k}}^{\lambda,\nu}, \quad (11b)$$

which is a system of two non-linear equations for the two parameters  $\lambda_d$  and  $\lambda_m$ . These have to be solved together with

$$\frac{1}{\beta} \sum_{\mathbf{k}} G_{\mathbf{k}}^{\lambda,\nu} \stackrel{!}{=} \frac{n}{2}, \quad (12)$$

which determines the chemical potential  $\mu_{\text{DGA}}$  in

$$G_{\mathbf{k}}^{\lambda,\nu} = \frac{1}{i\nu + \mu_{\text{DGA}} - \epsilon_{\mathbf{k}} - \Sigma_{\mathbf{k}}^{\lambda,\nu}} \quad (13)$$

to fix the required density  $n$ .

In practice, the determination of  $\lambda_d$  and  $\lambda_m$  is carried out using a specific variant of the Newton method. Let us, however, illustrate the solution process in a more transparent way which allows for a better understanding of its physical content. First, we use only the Pauli principle via Eq. (11a), to calculate  $\lambda_m$  for a given  $\lambda_d$ <sup>58</sup>. The pairs  $[\lambda_d, \lambda_m(\lambda_d)]$  are then used to calculate the potential energies at the one- and the two-particle level on the right and left hand side of Eq.(11b), respectively, as functions of  $\lambda_d$ . Furthermore, a chemical potential  $\mu_{\text{DGA}}$  is obtained for each pair. A solution of this equation corresponds to the specific value of  $\lambda_d$  for which  $E_{\text{pot}}^{(2)} - E_{\text{pot}}^{(1)} = 0$ . To illustrate the solution process visually we show in Fig. 1 this difference between the two potential energies as a function of  $\lambda_d$  for four different values of the filling at the interaction and temperature indicated by the red square in Fig. 2 (for the explicit values see the caption of Fig. 1 and Sec. III A). We clearly observe a crossing of all curves with the  $\lambda_d$ -axis where the  $\lambda_d$  value at this crossing corresponds to the solution of Eqs. (11).

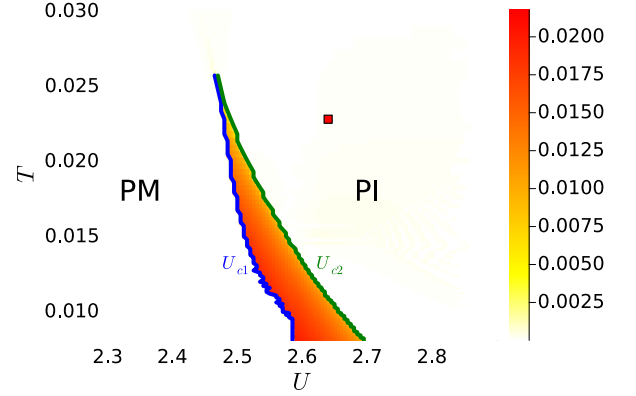


FIG. 2. DMFT paramagnetic phase diagram of the two-dimensional Hubbard model on a square lattice with nearest ( $t$ ), next-nearest ( $t'$ ), and next-to-next-nearest ( $t''$ ) neighbor hopping, plotted as a function of interaction strength  $U$  and temperature  $T$  at half-filling. Hysteresis is visualized via color coding, representing the difference in double occupancy  $d$  obtained from the metallic and insulating solutions, respectively.  $U_{c1}$  (blue line) and  $U_{c2}$  (green line) are the boundaries between the coexistence region and the paramagnetic metallic (PM) and paramagnetic insulating (PI) phases, respectively. The red dot marks the parameter set ( $U = 2.64$  and  $\beta = 44$ ) used to explore the system away from half-filling. Model parameters:  $t = 0.25$ ,  $t' = -0.075$ , and  $t'' = 0.05$ .

Interestingly, the solutions  $\lambda_d$  are monotonously decreasing with increasing filling, indicating that nonlocal correlations affect charge fluctuations in very different ways for different electron occupation numbers. This will be discussed in more detail in Sec. III A.

Let us finally note that, in the original version of the  $\lambda$  corrected IDGA<sup>55</sup> method, only Eq. (11a), which enforces the Pauli principle, was considered. Therefore only the spin susceptibility was rescaled, i.e., in our notation,  $\lambda_m \neq 0$  and  $\lambda_d = 0$ , with the charge renormalization only being included recently<sup>58</sup>. To distinguish between these two cases, we refer to the approach where both charge and spin susceptibilities are rescaled as IDGA<sub>dm</sub>, and to the version where only the spin susceptibility is rescaled as IDGA<sub>m</sub>.

### III. RESULTS

#### A. Charge susceptibility

To set the stage we have first mapped out the  $U$  vs.  $T$  phase diagram of the Hubbard model for the selected hopping parameters  $t$ ,  $t'$  and  $t''$  detailed in Sec. II A at half filling ( $n = 1$ ). The corresponding results are shown

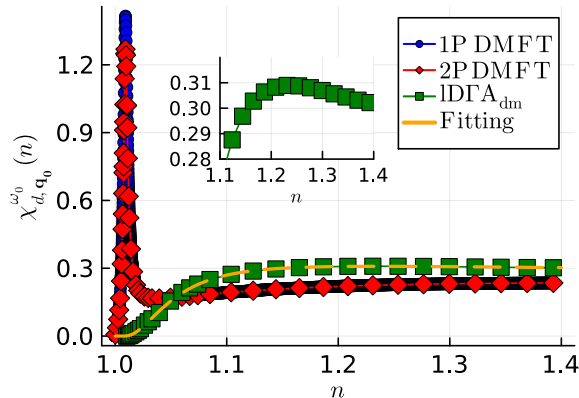


FIG. 3. Uniform charge susceptibility  $\chi_{d,\mathbf{q}_0=0}^{\omega_0=0}$  for  $U = 2.64$  and  $\beta = 44.0$  (see red square in Fig. 2) as a function of filling  $n$  obtained from DMFT (red diamonds) and ID $\Gamma A_{dm}$  (green squares). For comparison also  $\frac{1}{2} \frac{dn}{d\mu}$  is depicted (blue circles) which is equivalent to the uniform charge susceptibility within DMFT. The orange curve is obtained by fitting ID $\Gamma A_{dm}$  data using Eq. (A1) in appendix A with the fitting parameters are  $A = 0.6307$ ,  $B = 0.0658$ , and  $C = 0.1473$ . Inset: Zoom of the ID $\Gamma A_{dm}$  uniform charge susceptibility around its maximum value.

in Fig. 2 where the difference between the double occupancy  $\langle n_{\uparrow}n_{\downarrow} \rangle$  of the metallic and insulating solution is depicted as a heat map. This difference is obviously zero if only one of the phases exists [which is the paramagnetic metal (PM) for small values of  $U$  and the paramagnetic insulator (PI) for large values of  $U$ ] and takes finite values in the *coexistence region* where the self-consistent DMFT iteration has two fixed points, i.e., a metallic and an insulating one which obviously have different double occupancies. Note that exactly at half-filling charge fluctuations are typically strongly suppressed in the insulating phase on the right hand side of the coexistence region.

We now aim at finding a point in the phase diagram where the uniform charge susceptibility of DMFT is continuous as a function of the filling  $n$  and shows a pronounced peak close to  $n = 1$ . To this end, we have to avoid parameter sets  $(U, T)$  where the filling  $n$  as a function of the chemical potential  $\mu_{DMFT}$  displays a discontinuity. As is well known<sup>38,66–69</sup>, such behavior occurs just at the first-order metal–Mott insulator transition where the system features a finite jump in the occupation  $n$  as a function of  $\mu_{DMFT}$ . Therefore, we have considered an interaction and a temperature slightly away from the metal–insulator transition in the half filled model which is indicated by the red square in Fig. 2 and corresponds to  $U = 2.64$  and  $\beta = 44$ . Let us, however, note that also other points on the Mott insulating side of the phase diagram are possible for our analysis as long as the charge susceptibility is a continuous function of the chemical potential  $\mu_{DMFT}$ .

We now investigate how nonlocal correlations affect charge fluctuations for different densities  $n$ . To this end, we analyze the uniform charge susceptibility  $\chi_{d,\mathbf{q}_0}^{\omega_0}$ , where  $\omega_0 = 0$  and  $\mathbf{q}_0 = (0, 0)$ , which has been obtained in three different ways in Fig. 3: First we have evaluated the DMFT charge susceptibility obtained via Eqs. (4) and (6a) at  $\omega = \omega_0$  and  $\mathbf{q} = \mathbf{q}_0$  as a function of  $n$  which is shown by red diamonds in Fig. 3. While at and (very) close to half filling this correlation function is very small it gets strongly enhanced for finite (but still small) doping reaching a maximum around  $n \approx 1.01$ . For larger values of the doping it rapidly decays and starts to depend only weakly on  $n$  for  $n > 1.2$  where  $\chi_{d,\mathbf{q}_0}^{\omega_0} \approx 0.3$ . To confirm these results we have also calculated the compressibility  $\kappa = \frac{1}{n^2} \frac{dn}{d\mu}$  which is proportional to the uniform charge susceptibility ( $\chi_{d,\mathbf{q}_0=0}^{\omega_0=0} = \frac{1}{2} n^2 \kappa$ ) for a conserving theory such as DMFT. The corresponding results are given by blue circles in Fig. 3 and indeed show an excellent agreement with the results obtained from the charge susceptibility (except for very small deviations at the peak which can be attributed to the finite-difference approximation used in the numerical evaluation of the derivative  $\frac{dn}{d\mu}$ ).

As discussed in the introduction, DMFT captures local fluctuations accurately but neglects nonlocal correlations (or, more precisely, treats them only on a mean field level). To account for the latter, we have performed ID $\Gamma A_{dm}$  calculations for  $\chi_{d,\mathbf{q}}^{\lambda_{d,\omega}}$  as a function of the density  $n$ . Our results, shown as green squares in Fig. 3, demonstrate that nonlocal correlations have a pronounced effect on charge fluctuations. Close to half filling the peak in the uniform charge susceptibility  $\chi_{d,\mathbf{q}_0}^{\lambda_{d,\omega_0}}$  observed within DMFT is strongly suppressed in ID $\Gamma A_{dm}$ . As the filling increases, the rescaled susceptibility  $\chi_{d,\mathbf{q}_0}^{\lambda_{d,\omega_0}}$  becomes larger and eventually exceeds the corresponding DMFT value for  $n \gtrsim 1.0544$ . It reaches a maximum at around  $n_{\max} \approx 1.24$  (see inset of Fig. 3) and decays for larger  $n > n_{\max}$  eventually approaching the DMFT results. This is indeed the expected behavior as with increasing filling correlation effects become in general gradually weaker. Our results have a clear cut physical interpretation: Close to half-filling, the neglect of nonlocal correlations in DMFT leads to a substantial overestimation of uniform charge fluctuation whereas (far) away from  $n = 1$  DMFT underestimates them. Within our ID $\Gamma A_{dm}$  approach this effect can be interpreted as a rebalancing of charge and spin fluctuations induced by consistency relations (11) which mimics a fully self-consistent parquet treatment at substantially lower numerical cost. More specifically, the dominance of antiferromagnetic spin fluctuations in this filling regime, which is also indicated by a very large spin susceptibility in Fig. 7, leads to a localization of electrons by the formation of antiferromagnetic domains where charge fluctuations are strongly suppressed. On the contrary, for larger values of  $n$  the electron (or rather hole) mobility is increased as more free lattice sites (without holes) are available.



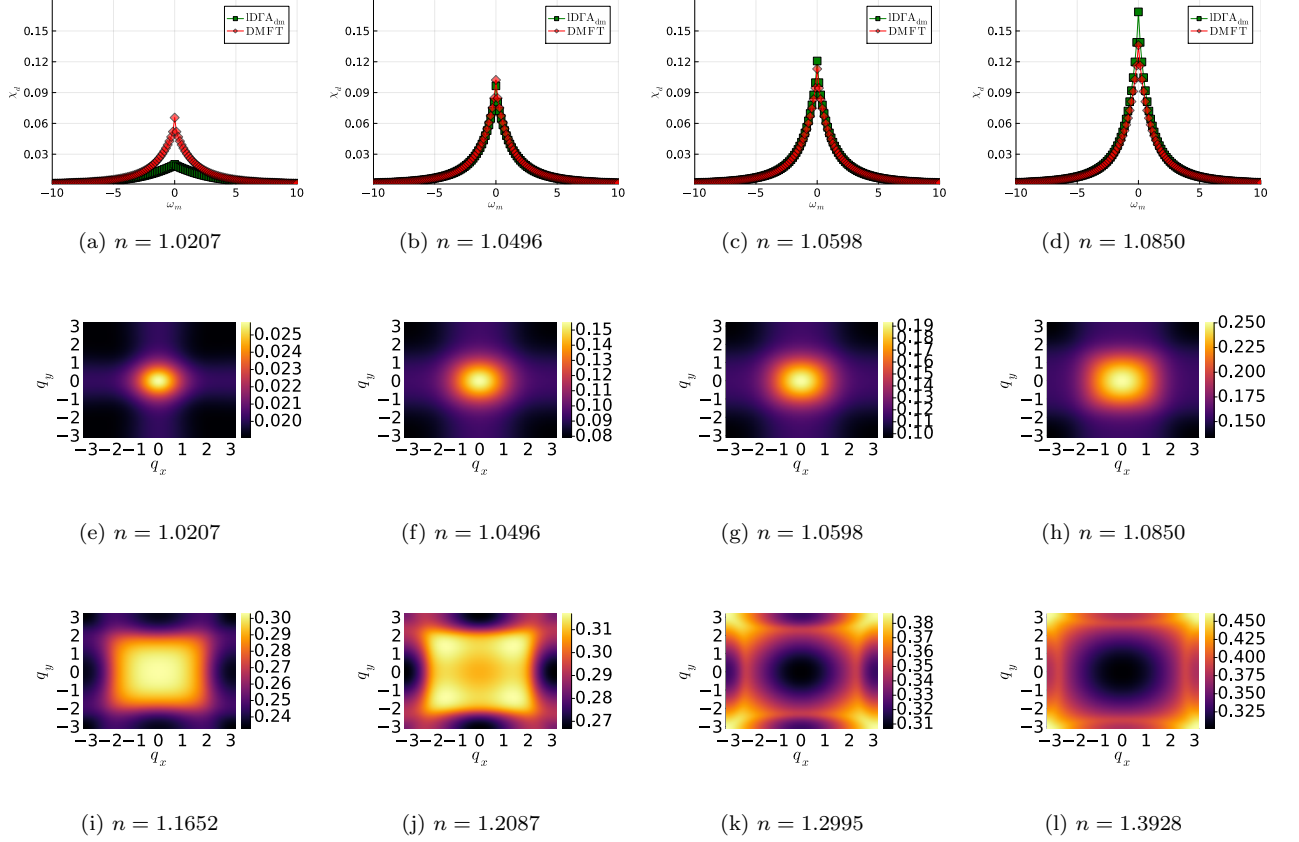


FIG. 4. Upper row: Local (momentum summed) charge susceptibility  $\sum_{\mathbf{q}} \chi_{\mathbf{d}, \mathbf{q}}^{\lambda_{\mathbf{d}}, \omega}$  of DMFT ( $\lambda_{\mathbf{d}}=0$ , red diamonds) vs. IDΓA<sub>dm</sub> ( $\lambda_{\mathbf{d}} \neq 0$ , green squares) as a function of the bosonic Matsubara frequency  $\omega$  for four different values of filling  $n$  gradually increasing from panel (a) to panel (d); Lower rows: static IDΓA<sub>dm</sub> charge susceptibility  $\chi_{\mathbf{d}, \mathbf{q}}^{\lambda_{\mathbf{d}}, \omega=0}$  as a function of momentum  $\mathbf{q}$  for eight different values of  $n$  gradually increasing from panel (e) to panel (l). Interaction strength and temperature are the same as in Fig. 3.

To get further insights into the impact of nonlocal correlations on charge fluctuations we have also investigated the frequency and momentum dependence of the charge susceptibility  $\chi_{\mathbf{d}, \mathbf{q}}^{\lambda_{\mathbf{d}}, \omega}$  in Fig. 4. In the upper panels (a)-(d) of this figure, we analyze the momentum-summed susceptibility  $\chi_{\mathbf{d}}^{\lambda_{\mathbf{d}}, \omega} = \sum_{\mathbf{q} \in \text{BZ}} \chi_{\mathbf{d}, \mathbf{q}}^{\lambda_{\mathbf{d}}, \omega}$  as a function of the bosonic Matsubara frequency  $\omega$  obtained by DMFT ( $\lambda_{\mathbf{d}}=0$ , red diamonds) and IDΓA<sub>dm</sub> ( $\lambda_{\mathbf{d}} \neq 0$ , green squares) for four different fillings. As expected, all curves show a pronounced peak at  $\omega = 0$  as classical fluctuations are typically dominant at finite temperatures. The doping dependence of the local (momentum summed) susceptibility follows the one observed for the uniform susceptibility in Fig. 3: Close to half filling [panel (a),  $n = 1.0207$ ] nonlocal correlations substantially reduce the DMFT susceptibilities which is also indicated by the large positive value of  $\lambda_{\mathbf{d}}$  at which  $E_{\text{pot}}^{(2)} - E_{\text{pot}}^{(1)} = 0$  for this filling in Fig. 1. At fillings  $n = 1.0496$  [panel (b)] and  $n = 1.0598$  [panel (c)], which lie close to  $n \simeq 1.0544$ , where the DMFT and IDΓA<sub>dm</sub> uniform charge susceptibilities coincide in Fig. 3, we observe a similar agreement for their local

(momentum-summed) counterparts. For  $n = 1.0496$ , the maximum value obtained from IDΓA<sub>dm</sub> is slightly lower than that from DMFT, while for  $n = 1.0598$ , the situation is reversed. At even higher filling,  $n = 1.085$  [panel (d)], the local IDΓA<sub>dm</sub> susceptibility becomes significantly larger than the DMFT result. This behavior for  $n = 1.0598$  and  $n = 1.085$ , where the local IDΓA<sub>dm</sub> susceptibility exceeds the DMFT one, is consistent with the negative values of  $\lambda_{\mathbf{d}}$  at which  $E_{\text{pot}}^{(2)} - E_{\text{pot}}^{(1)}$  crosses zero in Fig. 1.

The momentum dependence of the IDΓA<sub>dm</sub> charge susceptibility at  $\omega = 0$  is shown in the middle and lower row (e)-(l) of Fig. 4. At low fillings we observe a sharp maximum at  $\mathbf{q} = (0, 0)$  which indicates that uniform charge fluctuations are dominant in this parameter regime although the overall size of the charge susceptibility is strongly suppressed due to the rebalancing between charge and spin channel discussed above. Upon increasing the filling this sharp feature broadens, becomes completely flat around  $n = 1.1652$  [panel (i)], shifts away from  $\mathbf{q}_0$  to some incommensurate wave vectors  $\mathbf{q}$  at  $n = 1.2087$  [panel (j)] and eventually moves to  $\mathbf{q} = (\pi, \pi)$  correspond-

ing to a checkerboard structure for the two largest fillings considered here [panels (k) and (l)]. This behavior can be understood as an effect similar to the superexchange entailing antiferromagnetic spin order at half filling: For fillings substantially larger than  $n = 1$  the system features a lot of double occupancies. Its total energy can be lowered by hopping processes which are, however, only possible if doubly occupied sites are next to a singly occupied sites which requires an alternating (checkerboard) type distribution of these two type of occupancies.

Let us point out that the consistency condition in Eq. (11a) forbids any charge or spin order at finite temperatures in two spatial dimensions when the charge and spin susceptibilities are obtained from DMFT. In fact, a DMFT susceptibility at a (finite) transition temperature is given by  $\chi_{r,\mathbf{q}}^{\omega=0} \sim \frac{1}{q^2}$  in the vicinity of  $\omega = \omega_0$  and  $\mathbf{q} = \mathbf{q}_0$ . This, however, would lead to a divergence of the corresponding momentum integral for sum rule (11a) is incompatible with the finite value on the right hand side of this equation. While this is in agreement with the Mermin-Wagner theorem for the three dimensional magnetic order parameter in two dimensions<sup>70</sup> for which any ordered state at finite temperature is destroyed by fluctuations, a finite-temperature divergence of the charge susceptibility is in principle possible in two dimensions. This can be compatible with condition (11a) only if one replaces DMFT by a more accurate starting point which takes into account a non-mean field critical exponents  $\eta > 0$  for which the integral over  $\sim \frac{1}{q^{2-\eta}}$  is finite. In our case we are sufficiently far away from the critical endpoint of DMFT (see phase diagram in Fig. 2) where the mean field exponent  $\eta=0$  is justified which entails the above described reduction of the charge susceptibility. It is, however, not excluded that sizable charge fluctuations can be found in other parameter regimes closer to the critical endpoint of the Mott transition or at very low temperatures which cannot be unambiguously identified within the combination of DMFT and IDFA<sub>dm</sub>. Future studies of this question can be relevant also to clarify a possible correlation-driven enhancement of electron-phonon coupling in strongly correlated electron systems.<sup>71–73</sup>

## B. Correlation length

In this section, we investigate the correlation length  $\xi_d$  of charge fluctuations as a function of the filling  $n$ .  $\xi_d$  is obtained from a fit of our numerical data for  $\chi_{d,\mathbf{q}}^{\omega=0}$  to the following Ornstein-Zernicke form<sup>74</sup>:

$$\chi_{r,\mathbf{q}}^{\omega=0} = \frac{A_d}{(\mathbf{q} - \mathbf{q}_{\max})^2 + \xi_d^{-2}}, \quad (14)$$

where  $\mathbf{q}_{\max}$  is the momentum at which the charge susceptibility takes its maximum. In Fig. 5 results are shown both for DMFT (red diamonds) and for the IDFA<sub>dm</sub> approach (green squares). The different background colors indicate different values of  $\mathbf{q}_{\max}$  where  $\chi_{d,\mathbf{q}}^{\omega=0}$  assumes its

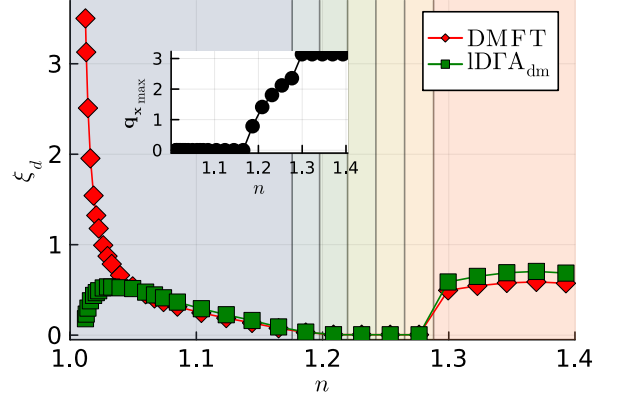


FIG. 5. The charge correlation length  $\xi_d$  as a function of filling  $n$  obtained from DMFT (red diamonds) and IDFA<sub>dm</sub> (green squares). Different  $\mathbf{q}_{\max}$  regions are shaded by different colors. Inset: The component  $q_x$  of  $\mathbf{q}_{\max}$  (where  $q_x = q_y$ ) as a function of the filling  $n$ . Parameters are the same as in Fig. 3.

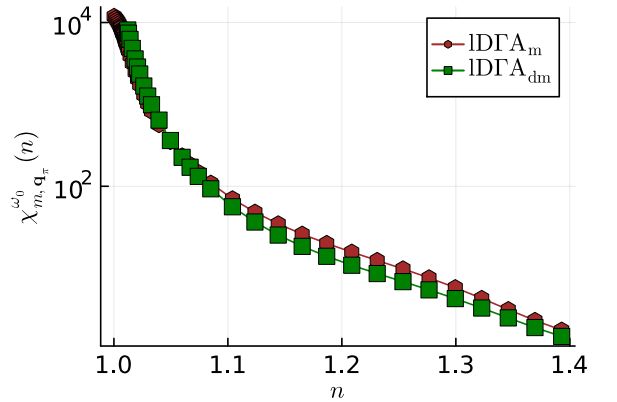


FIG. 6. Spin susceptibility  $\chi_{m,\mathbf{q}_\pi}^{\omega_0}$  as a function of filling  $n$  for IDFA<sub>m</sub> where only the magnetic channel is corrected ( $\lambda_m \neq 0$ ,  $\lambda_d = 0$ , brown hexagons) and for IDFA<sub>dm</sub> where we include both magnetic and charge corrections ( $\lambda_m \neq 0$ ,  $\lambda_d \neq 0$ , green squares). Here,  $\mathbf{q}_\pi = (\pi, \pi)$  denotes the antiferromagnetic ordering vector. Data are shown on a logarithmic scale on the  $y$ -axis for the same parameters  $U$  and  $T$  as in Fig. 3.

maximum. The specific values of  $\mathbf{q}_{\max}$  (or, more precisely, of the  $q_x$  component of  $\mathbf{q}_{\max}$  for  $q_y = q_x$ ) is depicted in the inset of Fig. 5 as a function of the filling  $n$ . In the case of DMFT the charge correlation length of uniform charge fluctuations  $\mathbf{q}_{\max} = (0, 0)$  is largest close to half-filling where also the corresponding susceptibility is strongly enhanced. Upon increasing the doping the correlation length rapidly decreases and eventually becomes negligible around  $n \approx 1.18$ . This is consistent with the broadening of the peak around  $\mathbf{q} = (0, 0)$  in

$\chi_{d,\mathbf{q}}^{\omega=0}$  with increasing doping observed in panels (e)-(i) of Fig. 4. At  $n \approx 1.18$  the maximum of  $\chi_{d,\mathbf{q}}^{\omega=0}$  changes from  $\mathbf{q} = (0,0)$  to an incommensurate value and eventually reaches  $\mathbf{q} = (\pi, \pi)$  at around  $n \approx 1.29$  indicating the dominance of a kind of checkerboard type order as discussed in the previous section.

Let us now compare these DMFT data to corresponding IDGA<sub>dm</sub> results. Close to half-filling the IDGA<sub>dm</sub> correlation length is significantly suppressed with respect to DMFT in accordance with the very small value of the associated susceptibility due to the mutual renormalization between spin and charge channels. Upon increasing  $n$  also the correlation length gets larger, reaches a maximum of  $\xi \simeq 0.5173$  at  $n \simeq 1.0330$  and eventually becomes slightly larger than the DMFT correlation length for fillings  $n > 1.0598$  which has been also observed for the susceptibility in Fig. 3. For even larger values of  $n$  the IDGA<sub>dm</sub> data closely follow the DMFT results where also the momentum vector at which the charge susceptibility attains its maximum changes at the same fillings as in DMFT. This can be easily understood by the fact a momentum independent  $\lambda$  correction can only rescale the entire DMFT charge susceptibility but is not able to invert its relative magnitude at different  $\mathbf{q}$  points.

### C. Spin susceptibility

We now turn our attention to the spin susceptibility  $\chi_{m,\mathbf{q}}^{\lambda_m,\omega}$  which probes magnetic fluctuations in the system. Although long-range antiferromagnetic order is absent in two dimensions at finite temperature due to the Mermin-Wagner theorem antiferromagnetic correlations remain the dominant mechanism in the repulsive Hubbard model. We therefore show in Fig. 6 the static antiferromagnetic susceptibility  $\chi_{m,\mathbf{q}\pi}^{\lambda_m,\omega=0}$  as a function of filling  $n$  where  $\mathbf{q}\pi = (\pi, \pi)$  is the antiferromagnetic ordering vector. Data are presented for IDGA<sub>m</sub> where  $\lambda_d = 0$  (brown hexagons) and IDGA<sub>dm</sub> where both spin and charge fluctuations are renormalized (green squares). In both cases the antiferromagnetic spin susceptibility exhibits a maximum at half filling and decreases monotonously with  $n$ . For  $n < 1.0544$  we observe larger values of  $\chi_{m,\mathbf{q}\pi}^{\lambda_m,\omega=0}$  for IDGA<sub>dm</sub> with respect to IDGA<sub>m</sub>. This is consistent with the fact that charge fluctuations are suppressed in this parameter regime via a positive  $\lambda_d$ . In fact, if  $\chi_{d,\mathbf{q}}^{\lambda_d,\omega=0}$  is reduced in Eq. (11a) by  $\lambda_d > 0$  we need a larger  $\chi_{m,\mathbf{q}}^{\lambda_m,\omega=0}$  to fulfill this consistency relation compared to the case of IDGA<sub>m</sub> where  $\lambda_d = 0$  which requires a stronger renormalization in the spin channel. The situation is reversed for  $n > 1.0544$  where  $\lambda_d < 0$ . In this case charge fluctuations are enhanced with respect to DMFT (see Fig. 3), which requires an even larger value of  $\lambda_m$  compared to IDGA<sub>m</sub> to fulfill

Eq. (11a). Hence, in this parameter regime IDGA<sub>dm</sub> predicts smaller spin fluctuations than the older IDGA<sub>m</sub> approach. This behavior nicely illustrates the rebalancing of spin and charge fluctuations which is achieved by enforcing the sum rule in Eq. (11b) in addition to Eq. (11a) in the framework of IDGA<sub>dm</sub>. This picture is also reflected in the frequency dependence of the local (momentum summed) antiferromagnetic spin susceptibility  $\chi_m^{\lambda_r,\omega} = \sum_{\mathbf{q}} \chi_{m,\mathbf{q}}^{\lambda_r,\omega}$  shown in the upper panels (a)-(d) of

Fig. 7 where for  $n < 1.0544$  [panels (a) and (b)] the peak at  $\omega = 0$  is larger for IDGA<sub>dm</sub> with respect to IDGA<sub>m</sub> while the opposite is true for  $n > 1.0544$  [panels (c) and (d)]. In the lower panel of Fig. 7 we depict the spin susceptibility at  $\omega = 0$  for four selected densities as a function of  $\mathbf{q} = (q_x, q_y)$ . We observe a maximum at the antiferromagnetic wave vector  $\mathbf{q} = \mathbf{q}\pi$ , confirming that antiferromagnetic spin fluctuations dominate near half-filling. For fillings beyond  $n > 1.35$ , the maximum shifts to  $\mathbf{q} = (\pi, 0)$  and  $\mathbf{q} = (0, \pi)$ , indicating a tendency toward stripe order.

Let us finally remark that we do not show any DMFT results for the (antiferromagnetic) spin susceptibility as this correlation function is already negative at  $\beta = 44$  which is an agreement with the antiferromagnetically ordered phase which DMFT predicts in this parameter regime.

### D. Self-energy

Next, we discuss the momentum-dependent self-energy of IDGA<sub>dm</sub> and compare it to the local one obtained from DMFT at four selected densities for which also the charge and spin susceptibilities are shown in Figs. 4 and 7. To provide an overview over the momentum dependence of this correlation function we show its imaginary part at the first positive Matsubara frequency  $\nu_0 = \frac{\pi}{\beta}$ ,  $\text{Im}\Sigma_{\mathbf{q}}^{\nu_0}$ , as a heat map in the  $(k_x, k_y)$  plane in Fig. 11 of appendix B. We are, however, particularly interested in this correlations function for  $\mathbf{k}$  points on the Fermi surface where the largest phase space for scattering between the electrons is available. In interacting systems, the Fermi surface is defined by the zeros of the real part of the retarded Green's function  $\text{Re}G_{\mathbf{k}}^{\omega}$  at zero (real) frequency  $\omega = 0$ . We, hence, define a renormalized dispersion as

$$E_{\mathbf{k}} = \epsilon_{\mathbf{k}} + \text{Re}\Sigma_{\mathbf{k}}^{\omega=0} \quad (15)$$

Where  $\text{Re}\Sigma_{\mathbf{k}}^{\omega}$  is the retarded self-energy as a function of real frequencies  $\omega$  which can be obtained from the associated Matsubara self-energy  $\Sigma_{\mathbf{k}}^{\nu}$  via an analytic continuation  $i\nu \rightarrow \omega$ . The Fermi surface is then determined by the condition  $E_{\mathbf{k}} = \mu_{\text{DFA}}$  where the chemical potential is determined via Eq. (12) to fix the density within IDGA<sub>dm</sub> to the desired value. Note, that in the non-bipartite case  $\mu_{\text{DFA}}$  typically differs from the corresponding chemical potential in DMFT as nonlocal correlations renormalize the energy scales in the system.



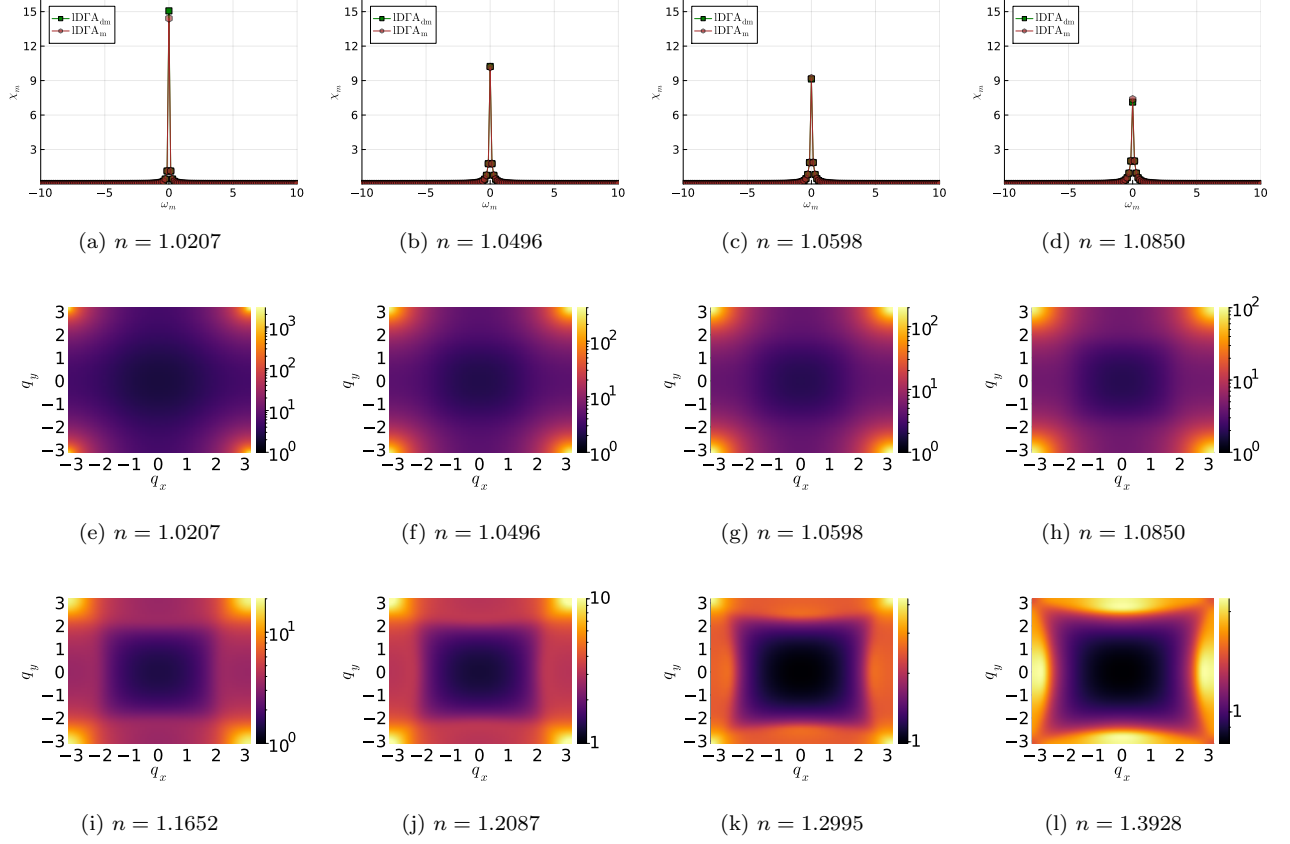


FIG. 7. Same as in Fig. 4 but for the spin susceptibility  $\chi_{m,q}^{\lambda,\omega}$  of IDΓA<sub>dm</sub> (green squares). In addition, we show data for the IDΓA<sub>m</sub> method (brown hexagon) where *only* the spin susceptibility is corrected by  $\lambda_m$  while  $\lambda_d=0$ .

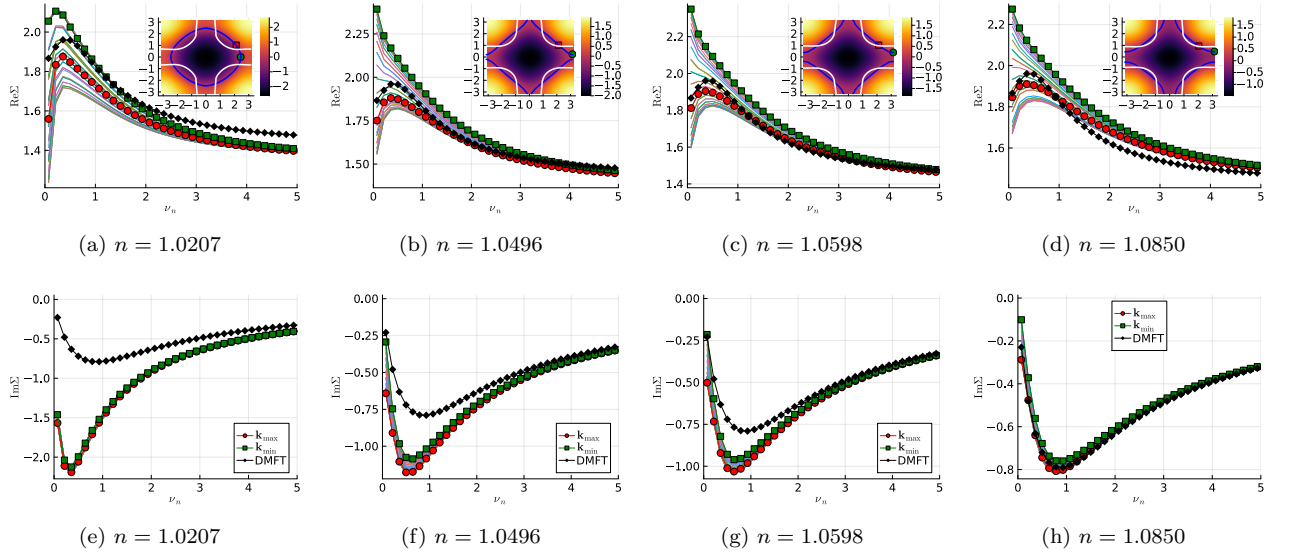


FIG. 8. Real (a)–(d) and imaginary (e)–(h) parts of the IDΓA<sub>dm</sub> self-energy for  $\mathbf{k}$ -points on the Fermi surface compared to the local DMFT self-energy (black diamond). Results for  $\mathbf{k}_{\max}$  and  $\mathbf{k}_{\min}$  are highlighted with a red circles and green squares, respectively. Inset [upper panels, (a)–(d)]: Color-coded interacting spectrum  $E_{\mathbf{k}} - \mu_{\text{D}\Gamma\text{A}}$ , as defined in Eq. (15).  $\mathbf{k}_{\min}$  and  $\mathbf{k}_{\max}$  points, which lie close to the antinodal and nodal points, respectively, are marked using the same symbols as in the self-energy plots. Calculation parameters are identical to those in Fig. 3.

In the upper row of Fig. 8 we show the real part of the Matsubara self-energy as a function of the Matsubara

frequency  $\nu$ . We have extrapolated these curves to zero frequency using a quadratic fit to obtain  $E_{\mathbf{k}}$  defined in Eq. (15). The insets show the function  $E_{\mathbf{k}} - \mu_{\text{DFA}}$  as a heat map in the  $(k_x, k_y)$  plane where we have indicated the interacting Fermi surface of IDFA<sub>dm</sub>, defined by  $E_{\mathbf{k}} - \mu_{\text{DFA}} = 0$ , with a blue solid line (for reference the Fermi surface of the non-interacting system is shown by a white solid line). We observe that while the Fermi surfaces for larger doping [panels (b), (c) and (d)] are all hole like (as the ones for the non-interacting system), an electron-like Fermi surface is found for the lowest doping  $n = 1.0207$  in panel (a). Such a Lifshitz type transition is purely driven by electronic correlations and has been also found in studies of the Hall conductivity of the Hubbard model in Refs. 75 and 76 where a change of majority charge carriers is signaled by a sign change of  $\sigma_{xy}$ .

To proceed with our discussion of the self-energy we have identified the two  $\mathbf{k}$  points on the Fermi surface,  $\mathbf{k}_{\text{max}}$  and  $\mathbf{k}_{\text{min}}$  where the absolute value of the imaginary part of the Matsubara self-energy  $\Sigma'_{\mathbf{k}}$  takes its maximum (red squares) and its minimum (green circles), respectively. Note that for the electron doped case considered here the maximum is closer to the so-called nodal point  $\mathbf{k} = (\frac{\pi}{2}, \frac{\pi}{2})$  while the minimum is in the vicinity of the antinodal point  $\mathbf{k} = (\pi, 0)$  which is the opposite behavior compared to the hole-doped case.<sup>77,78</sup> In the lower row of Fig. 8 we depict the imaginary part of the self-energy as function of the Matsubara frequency  $\nu$  for different momenta located on the Fermi surface between the maximum (red square) and the minimum (green circle). We clearly observe that close to half-filling [panel (e)] the absolute value of the imaginary part of the self-energy at the Fermi surface obtained from the IDFA<sub>dm</sub> calculations is significantly larger than that from DMFT. This can be attributed to the scattering of electrons at strong antiferromagnetic spin fluctuations which are observed at this filling (see Fig. 6). Upon increasing the doping to  $n = 1.0496$  [panel (f)] we observe a substantial increase in momentum differentiation which is consistent with the emergence of a pseudogap in this parameter regime (although for the definite identification of this feature the calculation of the full spectral function would be required). For an even larger doping of  $n = 1.0598$  in panel (g) we observe a very interesting effect: At the first Matsubara frequency, the minimal IDFA<sub>dm</sub> self-energy (green circle) becomes even *smaller* than the DMFT self-energy which indicates an enhancement of metallicity at this specific  $\mathbf{k}$  point. This is consistent with the fact that charge fluctuations start to get enhanced in IDFA<sub>dm</sub> with respect to DMFT at exactly this filling (see Fig. 3). This trend continues to the largest doping in panel (h) where the minimal self-energy of IDFA<sub>dm</sub> becomes smaller than the DMFT one at all Matsubara frequencies. Let us, however, note that for this doping value also the maximal self-energy is already rather close to its DMFT counterpart indicating that the effect of nonlocal correlations gradually decreases with increasing particle number.

Let us finally remark, that the IDFA self-energy ob-

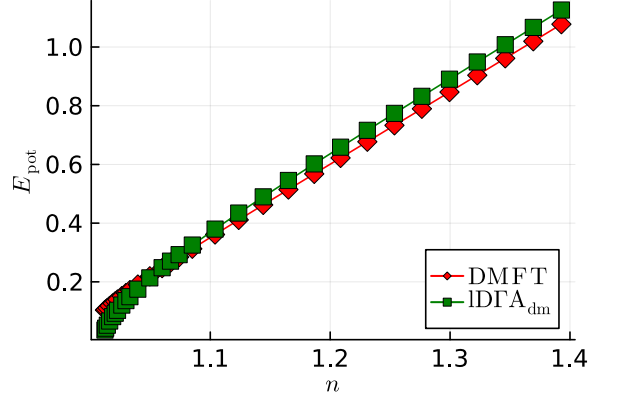


FIG. 9. Potential energy  $E_{\text{pot}}$  as a function of filling  $n$  obtained from DMFT (red diamonds) and IDFA<sub>dm</sub> (green squares). DMFT data are calculated at the one-particle level ( $E_{\text{pot}}^{(1)}$ ) while for IDFA<sub>dm</sub> the potential energies at the one- and two-particle levels are equivalent which is enforced by Eq. (11b). Parameters are the same as in Fig. 3.

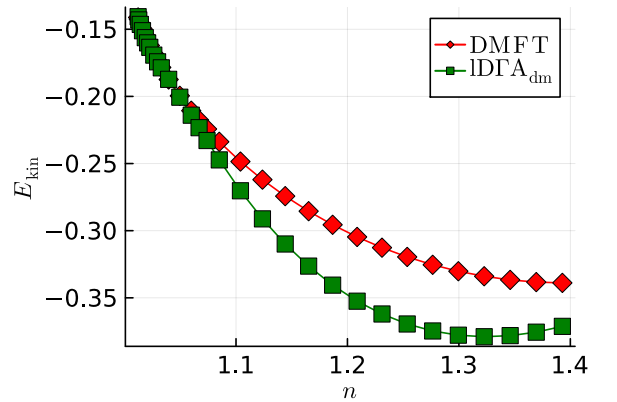


FIG. 10. Kinetic energy  $E_{\text{kin}}$  as a function of filling  $n$  obtained from DMFT (red diamonds) and IDFA<sub>dm</sub> (green squares). Parameters are the same as in Fig. 3.

tained via Eq. (7) can feature tiny violations of the correct high-frequency asymptotic behavior which makes some kind of tail correction necessary. While all qualitative (and also almost all quantitative) results of our calculations are unaffected by the concrete choice of the tail correction scheme, the height of the maximum of the uniform IDFA<sub>dm</sub> charge susceptibility as a function of  $n$  shown in the inset of Fig. 3 can change depending on the method used (while its location remains roughly at the same density  $n$ ). More technical details about the tail corrections of the self-energy will be provided in an upcoming paper Ref.<sup>79</sup>.

### E. Potential and kinetic energies

We finally discuss the behavior of the potential and kinetic energies of DMFT and IDGA<sub>dm</sub> as a function of filling which are shown in Figs. 9 and 10, respectively. As for the potential energy in Fig. 9, let us note that this thermodynamic observable can be calculated from the one-particle self-energy and Green's function ( $E_{\text{pot}}^{(1)}$ ) or from the two-particle spin and charge susceptibilities ( $E_{\text{pot}}^{(2)}$ ) [see Eq. (8b)]. For DMFT we present only  $E_{\text{pot}}^{(1)}$  since  $E_{\text{pot}}^{(2)}$  is not meaningful as we are already in the symmetry broken phase of this method where the spin susceptibility is negative which makes it unsuitable as an input for the calculation of other thermodynamic observables.<sup>57,80</sup> For the IDGA<sub>dm</sub> approach on the other hand the equality of both potential energies is enforced by our  $\lambda$  correction method. We observe that for low values of the doping the potential energy of IDGA<sub>dm</sub> is smaller than the corresponding DMFT result. This can be easily understood by the fact that strong spin fluctuations make the system more insulating in this parameter regime and, hence, suppress double occupancies of two electrons at one lattice site. Upon increasing the filling the IDGA<sub>dm</sub> potential energy gradually approaches the corresponding DMFT from below and eventually becomes larger at  $n = 1.0598$  where also larger charge fluctuations are predicted by IDGA<sub>dm</sub> with respect to DMFT. This result provides further evidence that at this filling nonlocal fluctuations lead to a delocalization of electrons which is not captured within the local DMFT approach. Such an interpretation is also supported by the behavior of the kinetic energy in Fig. 10. This thermodynamic variable is small (in absolute value) close to half-filling where correlation effects suppress the mobility of the particles and increases with increasing doping. This increase is stronger in IDGA<sub>dm</sub> compared to DMFT which again signals a delocalization of electrons due to nonlocal correlations.

## IV. CONCLUSION AND OUTLOOK

We have investigated the effect of nonlocal correlations in the two-dimensional Hubbard model as a function of (electron) doping for an interaction parameter and a temperature at which the system is a Mott insulator at half filling and DMFT predicts a substantial enhancement of uniform charge fluctuations for small doping. Our IDGA<sub>dm</sub> approach, which enforces a consistent evaluation of the potential energy from one- and two-particle quantities by means of an effective renormalization of DMFT charge and spin susceptibilities, predicts a strong suppression of these charge fluctuations by strong non-local antiferromagnetic spin fluctuations. This is a consequence of the rebalancing between these two types of fluctuations by the enforcement of sum rules for the Pauli principle and the potential energy within the IDGA<sub>dm</sub> approach. For larger fillings we observe the opposite trend

where nonlocal correlations induced by IDGA<sub>dm</sub> enhance the uniform charge fluctuations with respect to DMFT indicating an increase of the electron mobility. This scenario is also consistent with the large value of the antiferromagnetic susceptibility at half filling and its strong decay with increasing doping. The picture outlined above is also reflected in the correlation length which is strongly reduced in IDGA<sub>dm</sub> with respect to DMFT at small fillings  $n$ .

We also investigated the behavior of the self-energy at the Fermi surface. Close to half-filling, we find that the absolute value of the imaginary part of the self-energy  $\Sigma_{\mathbf{k}}^{\nu}$  obtained from IDGA<sub>dm</sub> is larger than that from DMFT for all  $\mathbf{k}$  points on the Fermi surface reflecting the impact of the strong nonlocal (spin) fluctuations on this correlation function. On the contrary, for  $n > 1.0544$  the imaginary part of the DMFT self-energy becomes larger than that from IDGA<sub>dm</sub> for some  $\mathbf{k}$  points. This again reflects the trend observed in the charge susceptibility where a metallization due to nonlocal correlations is found by IDGA<sub>dm</sub>. Finally, this picture is also confirmed by the analysis of the doping dependence of the potential and kinetic energies which also shows a suppression of electron mobility at low doping and a corresponding enhancement at larger fillings induced by nonlocal correlation.

It would be indeed very interesting to understand how nonlocal correlation effects and the consistent treatment of charge and spin fluctuations affect the physics of the two dimensional Hubbard model in a broader parameter regime. A particularly important question is how the consistent charge renormalization might affect the superconducting state at optimal doping as this can potentially guide the way how larger critical temperatures can be achieved. This is certainly a very interesting future research direction.

*Acknowledgements.* We thank A. Toschi and E. Moghadas for insightful discussions. We acknowledge financial support from the Deutsche Forschungsgemeinschaft (DFG) through Projects No. 407372336 and No. 449872909. The authors gratefully acknowledge the computing time granted by the Resource Allocation Board and provided on the supercomputers Lise and Emmy/Grete at NHR@ZIB and NHR@Göttingen as part of the NHR infrastructure. The calculations for this research were conducted with computing resources under the project hhp00048.

### Appendix A: Fitting function for $\chi_{\mathbf{d},\mathbf{q}_0}^{\lambda_{\mathbf{d}},\omega_0}$

The behavior of the susceptibility  $\chi_{\mathbf{d},\mathbf{q}_0}^{\lambda_{\mathbf{d}},\omega_0}$  as a function of filling  $n$  is well described by the following fit function:

$$\chi_{\mathbf{d},\mathbf{q}_0}^{\lambda_{\mathbf{d}},\omega_0} = \frac{A}{e^{\frac{B}{(n-1)(2-n)}} + e^{\frac{C}{(1-n)n}}}, \quad (\text{A1})$$

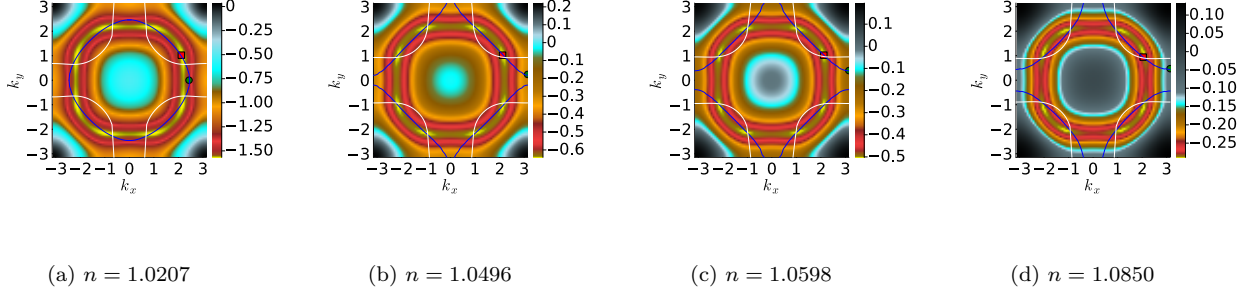


FIG. 11. Imaginary part of the self-energy for  $\nu = \nu_0 = \pi/\beta$  as a heat map in the  $(k_x, k_y)$  plane for four different fillings  $n$  in panels (a) to (d).  $\mathbf{k}_{\min}$  and  $\mathbf{k}_{\max}$  points, which lie close to the antinodal and nodal points, respectively, are marked using the same symbols as in the self-energy plots in Fig. 8. The blue lines indicate the Fermi surface predicted by 1DFA<sub>dm</sub> while the non-interacting Fermi surface is shown by white lines. Calculation parameters are identical to those in Fig. 3.

where  $A = 0.6307$ ,  $B = 0.0658$ , and  $C = 0.1473$ .

This somewhat elaborate functional form is motivated by the distinct behavior of the susceptibility near the limiting cases of the electronic filling  $n$ . Close to half-filling ( $|n - 1| \ll 1$ ), the susceptibility is exponentially suppressed. In this regime, a functional form of the type  $\chi_{\mathbf{d}, \mathbf{q}_0}^{\lambda_{\mathbf{d}}, \omega_0} \sim e^{-B/|n-1|}$  provides a reasonable approximation up to  $n \simeq 1.05$ . However, this simple form fails to capture the correct physical behavior further away from half-filling and, in particular, for the limits  $n \rightarrow 0$  and  $n \rightarrow 2$  where the susceptibility is expected to vanish. To account for this, we have modified the fitting function in the following way: To capture the suppression of the susceptibility near full filling ( $n \rightarrow 2$ ) a term of the form  $e^{-B/(n-1)(2-n)}$  is required. On the other hand, to correctly reproduce the behavior near empty filling ( $n \rightarrow 0$ ), a term proportional to  $e^{-C/(1-n)n}$  becomes necessary. Eq. (A1) effectively combines both limiting behaviors, providing an accurate fit across the full range of fillings which accurately describes our numerical data within  $n \in [1, 1.4]$ .

## Appendix B: Self-energy

In Fig. 11, we present the imaginary part of the self-energy,  $\Sigma_{\mathbf{k}}^{\nu}$  at the first positive Matsubara frequency  $\nu = \nu_0 = \pi/\beta$  for different electron fillings  $n$  as a heat

map in the  $(k_x, k_y)$  plane. As expected, we observe that the absolute value of the imaginary part of self-energy is largest at and near the Fermi surface where a relatively large phase space is available for scattering. This behavior is most pronounced close to half-filling for  $n \simeq 1.0207$  [panel (a)] where the Fermi surface is electron-like (see also discussion in the main text). For this small deviation of the electron density from  $n=1$ , the imaginary part of the self-energy remains negative for all momenta  $\mathbf{k}$ . Its absolute value is minimal at the edges of the Brillouin zone  $\mathbf{k} = (\pm\pi, \pm\pi)$  and increases upon approaching the Fermi surface where it takes its maximum values. Moving further to the center of the Brillouin zone  $\mathbf{k} = (0, 0)$  the magnitude of the self-energy again decreases which is compatible with the reduction of available phase space for scattering.

Upon increasing the filling  $n$  the (absolute value of the) imaginary part of the self-energy becomes smaller which is consistent with the fact that the system becomes gradually less correlated for increased doping [panels (b)-(d)]. At the Brillouin zone boundaries around  $\mathbf{q} \sim (\pi, \pi)$  we even observe an unphysical overshooting where the imaginary part of the Matsubara self-energy becomes negative corresponding to a violation of causality. This behavior, which indicates, that DfA is less reliable far away from the Fermi surface has been observed in previous works even for the full parquet based version of the method<sup>62</sup>.

<sup>1</sup> N. F. Mott, Rev. Mod. Phys. **40**, 677 (1968).

<sup>2</sup> K. Haule and G. L. Pascut, Scientific Reports **7**, 10375 (2017).

<sup>3</sup> B. H. Moon, Emergent Materials **4**, 989 (2021).

<sup>4</sup> Y. Fei, Z. Wu, W. Zhang, and Y. Yin, AAPS Bulletin **32**, 20 (2022).

<sup>5</sup> D. Chowdhury, A. Georges, O. Parcollet, and S. Sachdev, Rev. Mod. Phys. **94**, 035004 (2022).

<sup>6</sup> A. A. Patel, H. Guo, I. Esterlis, and

S. Sachdev, Science **381**, 790 (2023), <https://www.science.org/doi/pdf/10.1126/science.abq6011>.

<sup>7</sup> A. Georges, L. d. Medici, and J. Mravlje, Annual Review of Condensed Matter Physics **4**, 137 (2013).

<sup>8</sup> C. F. Hirjibehedin, Nature Nanotechnology **10**, 914 (2015).

<sup>9</sup> L. de' Medici, "The physics of correlated insulator, metals and superconductors," (Forschungszentrum Jülich GmbH, Institute for Advanced Simulations, 2017) Chap. Hund's metals explained, pp. 14.1–14.22.

- <sup>10</sup> P. W. Anderson, *Science* **177**, 393 (1972).
- <sup>11</sup> T. Moriya, *Spin Fluctuations in Itinerant Electron Magnetism*, Springer Series in Solid-State Sciences, Vol. 56 (Springer-Verlag, Berlin, Heidelberg, 1985).
- <sup>12</sup> T. Das, J.-X. Zhu, and M. J. Graf, *Journal of Materials Research* **28**, 659 (2013).
- <sup>13</sup> T. Schäfer, N. Wentzell, F. Šimkovic, Y.-Y. He, C. Hille, M. Klett, C. J. Eckhardt, B. Arzhang, V. Harkov, F. m. c.-M. Le Régent, A. Kirsch, Y. Wang, A. J. Kim, E. Kozik, E. A. Stepanov, A. Kauch, S. Andergassen, P. Hansmann, D. Rohe, Y. M. Vilk, J. P. F. LeBlanc, S. Zhang, A.-M. S. Tremblay, M. Ferrero, O. Parcollet, and A. Georges, *Phys. Rev. X* **11**, 011058 (2021).
- <sup>14</sup> N. Bergeal, J. Lesueur, M. Aprili, G. Faini, J. P. Contour, and B. Leridon, *Nature Physics* **4**, 608 (2008).
- <sup>15</sup> T. A. Maier and D. J. Scalapino, *npj Quantum Materials* **4**, 30 (2019).
- <sup>16</sup> A. E. Böhmer, J.-H. Chu, S. Lederer, and M. Yi, *Nature Physics* **18**, 1412 (2022).
- <sup>17</sup> M. M. Korshunov and Y. N. Togushova, *JETP Letters* **119**, 310 (2024).
- <sup>18</sup> T. Kaneko and Y. Ohta, *Journal of the Physical Society of Japan* **94**, 012001 (2025), <https://doi.org/10.7566/JPSJ.94.012001>.
- <sup>19</sup> M. Karolak, M. Izquierdo, S. L. Molodtsov, and A. I. Lichtenstein, *Phys. Rev. Lett.* **115**, 046401 (2015).
- <sup>20</sup> P. A. Volkov, M. Ye, H. Lohani, I. Feldman, A. Kanigel, and G. Blumberg, *npj Quantum Materials* **6**, 52 (2021).
- <sup>21</sup> P. Hansmann, T. Ayral, L. Vaugier, P. Werner, and S. Biermann, *Phys. Rev. Lett.* **110**, 166401 (2013).
- <sup>22</sup> J. Hubbard, *Proceedings of the Royal Society of London. Series A, Mathematical and Physical Sciences* **276**, 238 (1963).
- <sup>23</sup> M. C. Gutzwiller, *Phys. Rev. Lett.* **10**, 159 (1963).
- <sup>24</sup> J. Kanamori, *Progress of Theoretical Physics* **30**, 275 (1963), <https://academic.oup.com/ptp/article-pdf/30/3/275/5278869/30-3-275.pdf>.
- <sup>25</sup> N. Physics, *Nature Physics* **9**, 523 (2013).
- <sup>26</sup> H. Bethe, *Z. Phys.* **71**, 205 (1931).
- <sup>27</sup> F. H. L. Essler, H. Frahm, F. Göhmann, A. Klümper, and V. E. Korepin, *The One-Dimensional Hubbard Model* (Cambridge University Press, 2005).
- <sup>28</sup> S. R. White, *Phys. Rev. Lett.* **69**, 2863 (1992).
- <sup>29</sup> S. R. White, *Phys. Rev. B* **48**, 10345 (1993).
- <sup>30</sup> U. Schollwöck, *Annals of Physics* **326**, 96 (2011), january 2011 Special Issue.
- <sup>31</sup> A. Georges, G. Kotliar, W. Krauth, and M. J. Rozenberg, *Rev. Mod. Phys.* **68**, 13 (1996).
- <sup>32</sup> W. Metzner and D. Vollhardt, *Phys. Rev. Lett.* **62**, 324 (1989).
- <sup>33</sup> D. Vollhardt, K. Byczuk, and M. Kollar, “Dynamical mean-field theory,” in *Strongly Correlated Systems: Theoretical Methods*, edited by A. Avella and F. Mancini (Springer Berlin Heidelberg, Berlin, Heidelberg, 2012) pp. 203–236.
- <sup>34</sup> M. Imada, A. Fujimori, and Y. Tokura, *Rev. Mod. Phys.* **70**, 1039 (1998).
- <sup>35</sup> G. Rohringer and A. A. Markov, “Orbital magnetic field driven metal-insulator transition in strongly correlated electron systems,” (2024), [arXiv:2406.18729](https://arxiv.org/abs/2406.18729) [cond-mat.str-el].
- <sup>36</sup> P. A. Lee, N. Nagaosa, and X.-G. Wen, *Rev. Mod. Phys.* **78**, 17 (2006).
- <sup>37</sup> G. Kotliar, S. Murthy, and M. J. Rozenberg, *Phys. Rev. Lett.* **89**, 046401 (2002).
- <sup>38</sup> R. Nourafkan, M. Côté, and A.-M. S. Tremblay, *Physical Review B* **99**, 035161 (2019), 1807.03855 [cond-mat].
- <sup>39</sup> M. Reitner, P. Chalupa, L. Del Re, D. Springer, S. Ciuchi, G. Sangiovanni, and A. Toschi, *Phys. Rev. Lett.* **125**, 196403 (2020).
- <sup>40</sup> A. Kowalski, M. Reitner, L. Del Re, M. Chatzieftheriou, A. Amaricci, A. Toschi, L. de’ Medici, G. Sangiovanni, and T. Schäfer, *Phys. Rev. Lett.* **133**, 066502 (2024).
- <sup>41</sup> A. I. Lichtenstein and M. I. Katsnelson, *Phys. Rev. B* **62**, R9283 (2000).
- <sup>42</sup> G. Kotliar, S. Y. Savrasov, G. Pálsson, and G. Biroli, *Phys. Rev. Lett.* **87**, 186401 (2001).
- <sup>43</sup> T. Maier, M. Jarrell, T. Pruschke, and M. H. Hettler, *Rev. Mod. Phys.* **77**, 1027 (2005).
- <sup>44</sup> M. H. Hettler, A. N. Tahvildar-Zadeh, M. Jarrell, T. Pruschke, and H. R. Krishnamurthy, *Phys. Rev. B* **58**, R7475 (1998).
- <sup>45</sup> M. H. Hettler, M. Mukherjee, M. Jarrell, and H. R. Krishnamurthy, *Phys. Rev. B* **61**, 12739 (2000).
- <sup>46</sup> A. N. Rubtsov, M. I. Katsnelson, and A. I. Lichtenstein, *Phys. Rev. B* **77**, 033101 (2008).
- <sup>47</sup> H. Hafermann, G. Li, A. N. Rubtsov, M. I. Katsnelson, A. I. Lichtenstein, and H. Monien, *Phys. Rev. Lett.* **102**, 206401 (2009).
- <sup>48</sup> G. Rohringer, H. Hafermann, A. Toschi, A. A. Katanin, A. E. Antipov, M. I. Katsnelson, A. I. Lichtenstein, A. N. Rubtsov, and K. Held, *Rev. Mod. Phys.* **90**, 025003 (2018).
- <sup>49</sup> E. A. Stepanov, E. G. C. P. van Loon, A. A. Katanin, A. I. Lichtenstein, M. I. Katsnelson, and A. N. Rubtsov, *Phys. Rev. B* **93**, 045107 (2016).
- <sup>50</sup> L. Peters, E. G. C. P. van Loon, A. N. Rubtsov, A. I. Lichtenstein, M. I. Katsnelson, and E. A. Stepanov, *Phys. Rev. B* **100**, 165128 (2019).
- <sup>51</sup> G. Rohringer, A. Toschi, H. Hafermann, K. Held, V. I. Anisimov, and A. A. Katanin, *Phys. Rev. B* **88**, 115112 (2013).
- <sup>52</sup> T. Ayral and O. Parcollet, *Phys. Rev. B* **92**, 115109 (2015).
- <sup>53</sup> T. Ayral and O. Parcollet, *Phys. Rev. B* **93**, 235124 (2016).
- <sup>54</sup> T. Ayral and O. Parcollet, *Phys. Rev. B* **94**, 075159 (2016).
- <sup>55</sup> A. A. Katanin, A. Toschi, and K. Held, *Phys. Rev. B* **80**, 075104 (2009).
- <sup>56</sup> A. Toschi, A. A. Katanin, and K. Held, *Phys. Rev. B* **75**, 045118 (2007).
- <sup>57</sup> G. Rohringer and A. Toschi, *Phys. Rev. B* **94**, 125144 (2016).
- <sup>58</sup> J. Stobbe and G. Rohringer, *Phys. Rev. B* **106**, 205101 (2022).
- <sup>59</sup> T. Schäfer, N. Wentzell, F. Šimkovic, Y.-Y. He, C. Hille, M. Klett, C. J. Eckhardt, B. Arzhang, V. Harkov, F. m. c.-M. Le Régent, A. Kirsch, Y. Wang, A. J. Kim, E. Kozik, E. A. Stepanov, A. Kauch, S. Andergassen, P. Hansmann, D. Rohe, Y. M. Vilk, J. P. F. LeBlanc, S. Zhang, A.-M. S. Tremblay, M. Ferrero, O. Parcollet, and A. Georges, *Phys. Rev. X* **11**, 011058 (2021).
- <sup>60</sup> K.-M. Tam, H. Fotsos, S.-X. Yang, T.-W. Lee, J. Moreno, J. Ramanujam, and M. Jarrell, *Phys. Rev. E* **87**, 013311 (2013).
- <sup>61</sup> C.-X. Chen and N. Bickers, *Solid State Communications* **82**, 311 (1992).
- <sup>62</sup> A. Valli, T. Schäfer, P. Thunström, G. Rohringer, S. Andergassen, G. Sangiovanni, K. Held, and A. Toschi, *Phys. Rev. B* **91**, 115115 (2015).
- <sup>63</sup> G. Li, N. Wentzell, P. Pudleiner, P. Thunström, and

- K. Held, Phys. Rev. B **93**, 165103 (2016).
- <sup>64</sup> N. Wentzell, G. Li, A. Tagliavini, C. Taranto, G. Rohringer, K. Held, A. Toschi, and S. Andergassen, Phys. Rev. B **102**, 085106 (2020).
- <sup>65</sup> F. Krien, A. I. Lichtenstein, and G. Rohringer, Phys. Rev. B **102**, 235133 (2020).
- <sup>66</sup> P. Werner and A. J. Millis, Phys. Rev. B **75**, 085108 (2007).
- <sup>67</sup> A. Liebsch, Phys. Rev. B **77**, 115115 (2008).
- <sup>68</sup> J. Steinbauer, L. de' Medici, and S. Biermann, Phys. Rev. B **100**, 085104 (2019).
- <sup>69</sup> G. Sordi, K. Haule, and A.-M. S. Tremblay, Phys. Rev. B **84**, 075161 (2011).
- <sup>70</sup> N. Mermin and H. Wagner, Phys. Rev. Lett. **17**, 1133 (1966).
- <sup>71</sup> Z. B. Huang, W. Hanke, E. Arrigoni, and D. J. Scalapino, Phys. Rev. B **68**, 220507 (2003).
- <sup>72</sup> J. Coulter and A. J. Millis, "Electron-phonon coupling in correlated materials: insights from the hubbard-holstein model," (2025), arXiv:2505.08081 [cond-mat.str-el].
- <sup>73</sup> E. Moghadas, M. Reitner, T. Wehling, G. Sangiovanni, S. Ciuchi, and A. Toschi, "Effective enhancement of the electron-phonon coupling driven by nonperturbative electronic density fluctuations," (2025), arXiv:2503.12113 [cond-mat.str-el].
- <sup>74</sup> L. S. Ornstein and F. Zernike, Proc. K. Ned. Akad. Wet. **17**, 793 (1914).
- <sup>75</sup> A. G. Rojo, G. Kotliar, and G. S. Canright, Phys. Rev. B **47**, 9140 (1993).
- <sup>76</sup> A. A. Markov, G. Rohringer, and A. N. Rubtsov, Phys. Rev. B **100**, 115102 (2019).
- <sup>77</sup> D. Sénéchal and A.-M. S. Tremblay, Phys. Rev. Lett. **92**, 126401 (2004).
- <sup>78</sup> P. Worm, M. Reitner, K. Held, and A. Toschi, Phys. Rev. Lett. **133**, 166501 (2024).
- <sup>79</sup> J. Stobbe, M. Leusch, I. Titvinidze, and G. Rohringer, "Tail correction of the self-energy," (2025), in preparation.
- <sup>80</sup> E. G. C. P. van Loon, F. Krien, H. Hafermann, E. A. Stepanov, A. I. Lichtenstein, and M. I. Katsnelson, Phys. Rev. B **93**, 155162 (2016).